



Polarization-dependent high-intensity Kapitza-Dirac effect in strong laser fieldsBirger Böning ,* Willi Paufler, and Stephan Fritzsche *Helmholtz-Institut Jena, D-07743 Jena, Germany**and Theoretisch-Physikalisches Institut, Friedrich-Schiller-Universität Jena, D-07743 Jena, Germany*

(Received 28 October 2019; accepted 19 February 2020; published 10 March 2020)

We study the deflection of photoelectrons in intense elliptically polarized standing light waves, known as the high-intensity Kapitza-Dirac effect. In order to compute the longitudinal momentum transfer to the photoelectron in above-threshold ionization, we utilize a complete description of the quantum dynamics in the spatially dependent field of the standing light wave. We propose experimental conditions under which low-energy photoelectrons can be generated with remarkably high longitudinal momenta that can be controlled via the polarization of the standing wave. We expect that future experimental realizations will provide additional insights into the momentum transfer in intense laser-atom interactions.

DOI: [10.1103/PhysRevA.101.031401](https://doi.org/10.1103/PhysRevA.101.031401)

The Kapitza-Dirac effect (KDE) for free electrons, atoms, and molecules has attracted much interest over the past decades owing to its great potential to advance matter optics [1–4]. Already in 1933, Kapitza and Dirac [5] suggested that free electrons should be deflected by an intense standing light wave due to an exchange of multiple photon momenta $\Delta p = n\hbar k$. Later experiments on the KDE [6,7] revealed two distinct scattering regimes [cf. Fig. 1(a)] that depend on the ponderomotive energy U_p of the standing wave and the energy $E_p = p^2/2$ of the electrons. In the Bragg regime, high-energy electrons ($E_p \gg U_p$) are deflected according to Bragg's law $n\lambda_e/\lambda = 2 \sin \vartheta$ with the de Broglie wavelength $\lambda_e = h/p$, whereas a diffraction pattern is formed behind the standing wave in the diffraction regime ($E_p \ll U_p$). In both regimes, the momentum transfer to the electron is in the order of one photon momentum $\hbar k$, making technical applications a challenge.

A (much) larger momentum transfer is achieved in the high-intensity KDE [Fig. 1(b)], first observed by Bucksbaum *et al.* [8]. Instead of a free-electron source, neutral atoms are placed within the standing wave and photoelectrons are generated by above-threshold ionization (ATI). These electrons are emitted narrowly around the polarization plane with distinct energies spaced by $\hbar\omega$, and are then scattered in the continuum before they reach the detector with longitudinal momenta up to the order $1000\hbar k$. For photoelectrons with fixed energy, the polar-angle distribution (PAD) therefore shows distinct maxima away from the polarization plane [Fig. 1(d)].

The momentum transfer in the high-intensity KDE can be understood in terms of the semiclassical photoelectron dynamics in the effective ponderomotive potential of the standing wave [8]. A more sophisticated quantum-mechanical treatment should be based on the strong-field approximation (SFA) in order to account for the laser field in the continuum (Volkov) states available to the photoelectron [9–11]. However, in contrast to the ATI with traveling waves, where

the momentum transfer to the photoelectron is small [12–14] and it is often sufficient to use the dipole approximation, *nondipole* contributions to the laser-electron interaction need to be considered for the ATI in standing waves. This need arises from the particular spatial dependence of a standing wave.

In one SFA-based approach, the laser field is quantized and transitions from the resulting QED-Volkov states to free-electron states are included [15]. The momentum transfer in the high-intensity KDE with circularly polarized standing waves can then be explained, and also the free-electron KDE can be reproduced [16,17]. In a second approach, the laser field is treated classically. Then nondipole Volkov states exist that account for the spatial dependence of the field in the photoelectron dynamics [18,19]. Since a standing wave is formed by two counterpropagating laser modes, the corresponding Volkov states exhibit phase singularities due to the (multiple) absorption of photons from one mode and reemission into the other, known as virtual Compton scattering. In this scattering process, the photoelectron energy remains constant, while its momentum changes by an integer multiple of $2\hbar k$. This results in the large momentum transfer in the high-intensity KDE for linear polarization [20].

Until now, most studies of the high-intensity KDE have focused on high-energy ($E_p > U_p$) photoelectrons, similar to the Bragg regime in the free-electron KDE. Moreover, while elliptically polarized standing waves have been studied in the free-electron KDE [21,22], only linear and circular polarizations were considered in the high-intensity KDE. However, standing light waves with elliptical polarization [23] and also high intensities [24] can nowadays be routinely generated, which allow the observation of low-energy photoelectrons with $E_p < U_p$.

In this Rapid Communication, we theoretically study the high-intensity KDE in *elliptically* polarized standing waves [Fig. 1(c)] and analyze the momentum transfer to low- and high-energy photoelectrons. Based on the SFA and the use of nondipole Volkov states, we here demonstrate that low-energy photoelectrons exhibit markedly different PADs when

*birger.boening@uni-jena.de

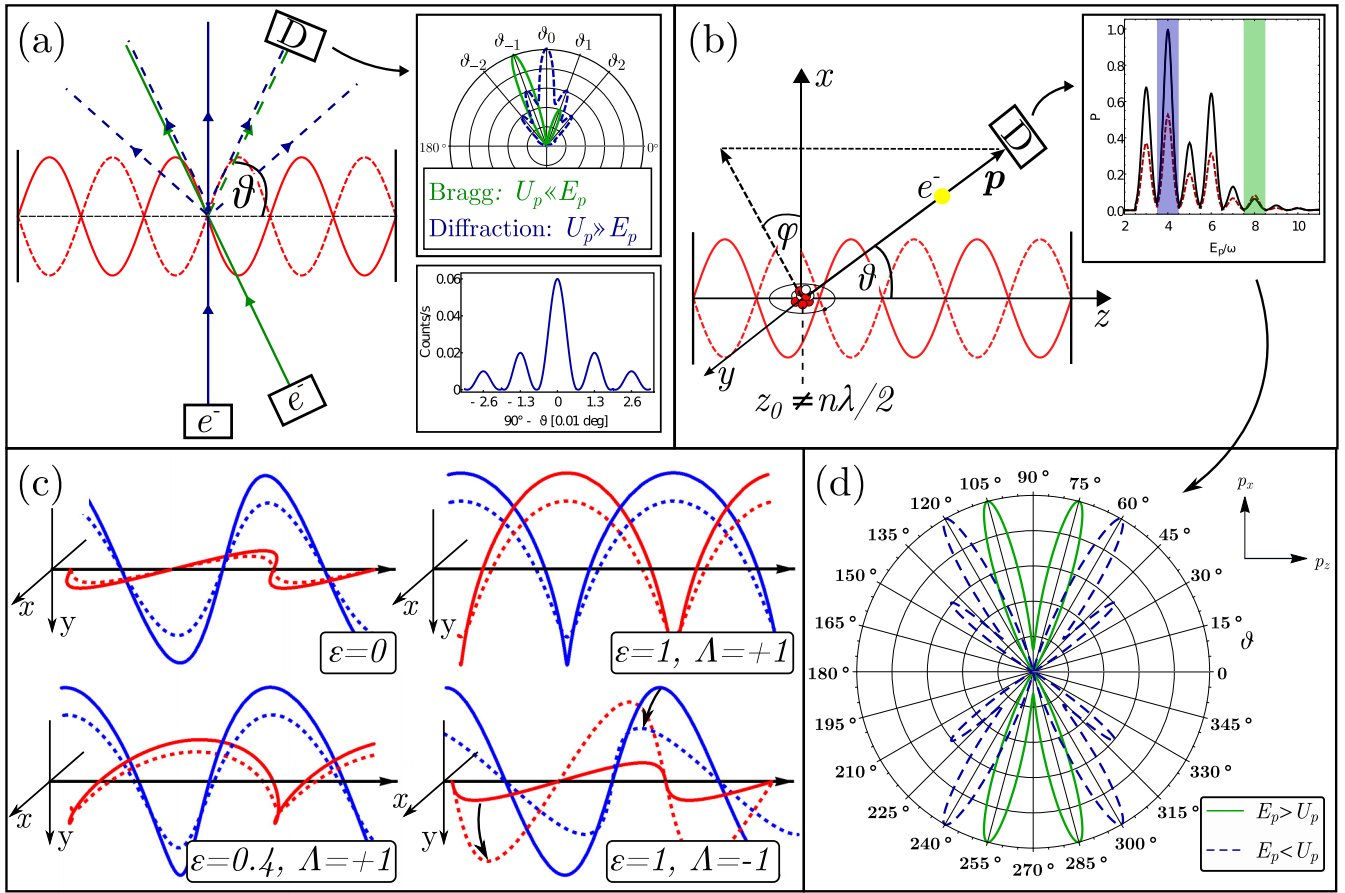


FIG. 1. Deflection of electrons in an intense standing light wave. (a) In the free-electron KDE, electrons with fixed kinetic energy $E_p = p^2/2$ are deflected by a standing light wave (red) and detected at D under an angle ϑ . In the Bragg regime ($U_p \ll E_p$) electrons are deflected according to Bragg's law (green solid line in the upper inset), while a diffraction pattern is formed for $U_p \gg E_p$ (blue dashed line and displayed with exaggerated angles), if the electrons enter perpendicularly to the standing wave. The lower inset shows the experimental PAD from Ref. [6] in the diffraction regime. (b) High-intensity KDE as considered in the present work: Neutral atoms are placed in a standing light wave of ellipticity ε at $z = z_0$ and ATI photoelectrons are emitted with momentum $\mathbf{p} = (p, \vartheta, \varphi)$. The inset shows typical ATI spectra for two values of ϑ (black solid and red dashed curves), if the detector D measures photoelectrons with energy $E_p = p^2/2$ under given polar and azimuthal angles ϑ and φ . The electron count for a given ATI peak as a function of ϑ yields the PADs [see (d)]. (c) Standing light waves of different ellipticities ε and relative orientations Λ ; shown are electric (red) and magnetic (blue) fields as functions of z and for two different times (solid: $t = 0$; dashed: $t = T_{\text{cycle}}/8$). (d) PADs of high-energy (green solid curves) and low-energy (blue dashed curves) photoelectrons in the high-intensity KDE. The maxima in the PADs correspond to much larger longitudinal momenta than in (a). The blue dashed curve illustrates our main finding: Low-energy photoelectrons have a significant probability to be emitted with very large longitudinal momenta, leading to a second set of maxima in their PAD.

compared to the high-energy photoelectrons considered in previous studies. It will be shown, in particular, that the momentum transfer to low-energy photoelectrons can be significantly enhanced [blue dashed curve in Fig. 1(d)] and controlled via the polarization of the standing wave. If not stated otherwise, we use atomic units throughout ($m_e = e = \hbar = 4\pi\varepsilon_0 = 1$).

To explore the PADs of photoelectrons from the ATI of atoms in a standing light wave, we describe the latter in terms of its vector potential $\mathbf{A}_\Lambda(\mathbf{r}, t)$. Using a Coulomb gauge, we write this vector potential as sum of two counterpropagating modes $\mathbf{A}^{(1)}(\mathbf{r}, t) = \tilde{A}_0[\cos(kz - \omega t)\mathbf{e}_x - \varepsilon \sin(kz - \omega t)\mathbf{e}_y]$ and $\mathbf{A}^{(2)}(\mathbf{r}, t) = \tilde{A}_0[-\cos(kz + \omega t)\mathbf{e}_x + \Lambda\varepsilon \sin(kz + \omega t)\mathbf{e}_y]$ with the amplitude $\tilde{A}_0 = A_0/\sqrt{1 + \varepsilon^2}$, the frequency $\omega = 2\pi c/\lambda$, the wave number $k = \omega/c$, the ellipticity $-1 \leq \varepsilon \leq 1$, as well as the relative orientation $\Lambda = \pm 1$ of the two

modes (counter-rotating for $\Lambda = -1$, corotating for $\Lambda = +1$). The intensity and ponderomotive energy of each individual mode are given by $I = A_0^2\omega^2 c/(8\pi)$ and $U_p = A_0^2/4$, respectively. With these definitions, the vector potential $\mathbf{A}_\Lambda(\mathbf{r}, t)$ for the two possible orientations $\Lambda = \pm 1$ can be written in the compact form,

$$\mathbf{A}_{+1}(\mathbf{r}, t) = 2\tilde{A}_0 \sin(\omega t)[\sin(kz)\mathbf{e}_x + \varepsilon \cos(kz)\mathbf{e}_y], \quad (1a)$$

$$\mathbf{A}_{-1}(\mathbf{r}, t) = 2\tilde{A}_0 \sin(kz)[\sin(\omega t)\mathbf{e}_x - \varepsilon \cos(\omega t)\mathbf{e}_y]. \quad (1b)$$

The corresponding electric $[\mathbf{E}(\mathbf{r}, t) = -\partial\mathbf{A}_\Lambda/\partial t]$ and magnetic $\mathbf{B}(\mathbf{r}, t) = \nabla \times \mathbf{A}_\Lambda$ fields are illustrated in Fig. 1(c). For $\mathbf{A}_{+1}(\mathbf{r}, t)$ the fields oscillate in time, while the field vectors have constant magnitude and rotate around the beam axis for $\mathbf{A}_{-1}(\mathbf{r}, t)$.

For the sake of simplicity, let us consider an atomic target in a hydrogenlike $1s$ initial state $|\Psi_0\rangle = |\Phi_0\rangle e^{i\mathbf{p}t}$, placed on the beam axis at position $z_0 \neq n\lambda/2$ within the standing wave [Fig. 1(b)]. The role of the target position is discussed in Appendix B. In order to compute PADs, we derive the transition amplitude T_p of an electron from the initial state $|\Psi_0\rangle$ to continuum *nondipole* Volkov states $|\chi_p(t)\rangle$. These Volkov states are approximate solutions to the Schrödinger equation for the photoelectron in the fields generated by the vector potential $\mathbf{A}_\Lambda(\mathbf{r}, t)$ and are characterized by the asymptotic photoelectron momentum $\mathbf{p} = (p, \vartheta, \varphi)$ at the detector. A general expression for $|\chi_p(t)\rangle$ was derived by us in Ref. [19], including v/c corrections to the dipole approximation. For the standing wave (1), the nondipole Volkov states can be written in terms of plane waves as (cf. Appendix A)

$$\chi_p(\mathbf{r}, t) = \frac{1}{(2\pi)^{3/2}} \sum_{N_1, N_2, N_{12}=-\infty}^{\infty} C_N(\mathbf{p}) e^{-i(E_N t - \mathbf{p}_N \mathbf{r})}, \quad (2)$$

where $N = (N_1, N_2, N_{12})$ and $C_N(\mathbf{p})$ are expansion coefficients that depend on \mathbf{p} as well as the parameters I, ε, Λ , and ω that define the vector potential. In expression (2), the energy and momentum of the individual plane waves are given by

$$E_N = E_p + 2\tilde{U}_p - (N_1 + N_2)\omega, \quad (3a)$$

$$\mathbf{p}_N = \mathbf{p} + \frac{2\tilde{U}_p p_z}{c\omega} \mathbf{k} - (N_1 - N_2)\mathbf{k} - 2N_{12}\mathbf{k}, \quad (3b)$$

respectively, with the photoelectron energy $E_p = p^2/2$ at the detector and $\tilde{U}_p = U_p/[1 - (p_z/c)^2]$.

The individual plane-wave contributions in Eq. (2) arise from the interaction of the photoelectron with the standing wave: The absorption of N_1 and N_2 photons from the laser modes $\mathbf{A}^{(1)}$ and $\mathbf{A}^{(2)}$ changes the photoelectron energy by $(N_1 + N_2)\omega$ and its momentum by $(N_1 - N_2)\mathbf{k}$, respectively. Moreover, the photoelectron may absorb N_{12} photons from one mode and emit the same number into the *other*, leaving its energy constant while changing its momentum by $2N_{12}\hbar\mathbf{k}$. This virtual Compton scattering leads to a momentum transfer Δp_z along the beam axis to a photoelectron emitted within a certain ATI peak and hence to the characteristic deflection of electrons in the high-intensity KDE.

The angle- and energy-differential ionization probability $\mathbb{P}(\mathbf{p}) = p|T_p|^2$ is then readily given in terms of the direct SFA transition amplitude [19],

$$\begin{aligned} T_p &= -i \int_{-\infty}^{\infty} dt \langle \chi_p(t) | \hat{V}_{le}(\mathbf{r}, t) | \Psi_0(t) \rangle \\ &= -2\pi i \sum_{N_1, N_2, N_{12}=-\infty}^{\infty} C_N(\mathbf{p}) V(\mathbf{p}_N) \delta(E_N + I_p), \end{aligned} \quad (4)$$

where $\hat{V}_{le}(\mathbf{r}, t) = \mathbf{A}(\mathbf{r}, t) \cdot \hat{\mathbf{p}} + 1/2A^2(\mathbf{r}, t)$ is the laser-electron interaction potential. Note that we neglected any rescattering between the photoelectron and parent ion in Eq. (4). This approximation is justified, since rescattering contributions are suppressed beyond the dipole regime [25,26]. In the above expression, the Dirac δ function defines the positions of the ATI peaks, which have relative amplitudes given by the coefficients $C_N(\mathbf{p})$ and the matrix element $V(\mathbf{p}) = \langle \mathbf{p} | V(\mathbf{r}) | \Phi_0 \rangle$ of the Coulomb potential $V(\mathbf{r})$. In the following, we restrict

our analysis to photoelectrons emitted in the p_x - p_z plane, i.e., the azimuthal angle $\varphi = 0$. Then, the PADs are given by the differential ionization probability $\mathbb{P}(\mathbf{p})$ as a function of the polar angle ϑ for a fixed energy $E_p = p^2/2$. Below, the PADs will exhibit several maxima at $\vartheta = \vartheta_{\max} \neq \pi/2$. We use these maxima to define the *momentum transfer* $\Delta p_z = \sqrt{2E_p} \cos \vartheta_{\max}$ to the photoelectron. When the photoelectron is emitted from the target atom, it interacts with the electromagnetic field of the standing wave and performs an oscillating motion in the longitudinal z direction [8] before it reaches the detector where the calculated PADs are measured.

As shown in Fig. 2(a), for a linearly polarized standing wave ($\varepsilon = 0$) of intensity $I = 5 \times 10^{13}$ W/cm² photoelectrons are preferably emitted with a particular momentum transfer $\Delta p_z \approx 560\hbar k$, yielding four maxima in the PAD symmetric to the polarization plane ($\vartheta = 90^\circ$). This splitting in four maxima is the high-intensity KDE [8]. The PADs have a similar shape for all photoelectron energies E_p and the angle ϑ_{\max} of maximum emission probability decreases with E_p . This results in a momentum transfer $\Delta p_z = \sqrt{2E_p} \cos \vartheta_{\max}$ that is independent of E_p and an angle ϑ_{\max} that follows the inverse square-root law $\cos \vartheta_{\max} \sim E^{-1/2}$ as obtained within the QED-Volkov approach [15].

The four maxima in the PAD of high-energy photoelectrons are also clearly discernible at higher laser intensities [red dashed curve in Fig. 2(b)], and correspond to a momentum transfer $\Delta p_z \approx 850\hbar k$. However, low-energy photoelectrons ($E_p < U_p$) exhibit a markedly different PAD [black solid curve in Fig. 2(b)], since now a second set of maxima appears that corresponds to $\Delta p_z \approx 1250\hbar k$. The emergence of additional maxima in the PADs was related to nondipole effects in the ionization with ultrashort pulses [27]. In the high-intensity KDE, however, this different behavior of low- and high-energy photoelectrons is one of the main findings of this work. We can understand the different PADs in terms of the ponderomotive force $\mathbf{F}_p(z) = U_p k \sin(2kz) \mathbf{e}_z$. On a photoelectron emitted along the polarization direction, \mathbf{F}_p induces an oscillating motion along the beam axis. For $E_p > U_p$, the motion of the photoelectron is not bound by the potential and can thus be described classically, leading to a distinct value of longitudinal momentum p_z at the detector [8]. For $E_p < U_p$, on the other hand, the electron cannot classically move over the potential crests and the plane-wave contributions with different p_z in expression (2) interfere, giving rise to another maximum in the PADs. In order to analyze this interference mechanism more closely, it might be instructive to perform quantum-trajectory Monte Carlo simulations in a future work. The above results show that in the high-intensity KDE, two distinct regimes exist for the PADs of low-energy photoelectrons with $E_p < U_p$ and of high-energy photoelectrons with $E_p > U_p$, quite analogous to the Bragg and diffraction regimes in the free-electron KDE [1]. In both regimes, the momentum transfer is determined by the magnitude $U_p k \sim I$ of the ponderomotive force. This is in line with our computations, which show a linear dependence of Δp_z on the intensity I [Fig. 2(c)].

To observe low-energy photoelectrons with $E_p < U_p$, experimental parameters can be estimated, since the ponderomotive potential has to be in the order of a few photon energies, $U_p = I\lambda^2/(2\pi c^3) \geq n\omega$. For example, if PADs of

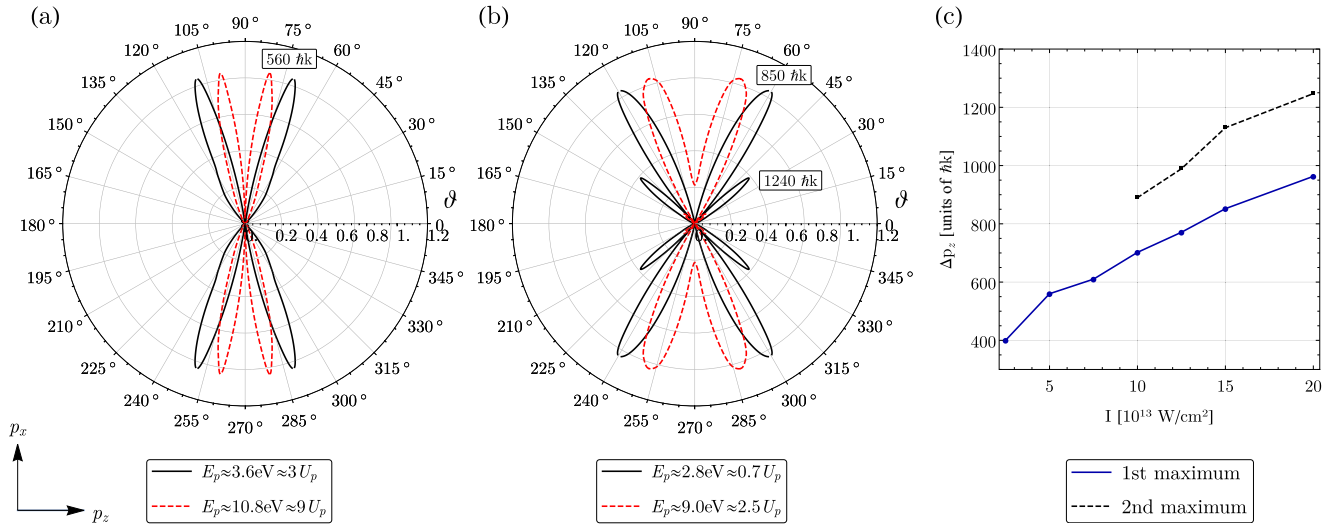


FIG. 2. Momentum transfer in the high-intensity KDE with linearly polarized standing light waves ($\varepsilon = 0$). PADs of photoelectrons with $E_p \approx 3\omega$ (black solid) and $E_p \approx 10\omega$ (red dashed) are shown in the left two panels for two intensities: (a) $I = 5 \times 10^{13} \text{ W/cm}^2$ and (b) $I = 15 \times 10^{13} \text{ W/cm}^2$. At low intensity ($U_p \approx \omega$), both PADs refer to high-energy photoelectrons ($E_p > U_p$) and have one set of maxima, with a momentum transfer $\Delta p_z \approx 560\hbar k$. At high intensity, in contrast, the red dashed curve represents high-energy photoelectrons and has one set of maxima ($\Delta p_z \approx 850\hbar k$), while the black solid curve represents low-energy photoelectrons ($E_p < U_p$) and has an additional set of maxima ($\Delta p_z \approx 1240\hbar k$). (c) Momentum transfer to photoelectrons with $E_p \approx 3\omega$, corresponding to the maxima in their PADs, as a function of the intensity. For $I \geq 10 \times 10^{13} \text{ W/cm}^2$, $E_p < U_p$ and the second set of maxima appears. The PADs in (a) and (b) are normalized to their respective maxima and the absolute magnitudes of the red dashed curves differ by a factor of (a) 0.93 and (b) 0.71, respectively, from the black solid curves. Parameters used: $\lambda = 1200 \text{ nm}$ ($\omega = 1.03 \text{ eV}$), $I_p = 14 \text{ eV}$ (krypton).

photoelectrons with $E_p \approx 3\omega$ can be measured reliably, the minimum intensity of the standing wave with wavelength λ must be

$$I_{\min} \left(\frac{\text{W}}{\text{cm}^2} \right) = 2.16 \times 10^{23} \times [\lambda(\text{nm})]^{-3}, \quad (5)$$

in order to resolve the second set of maxima in the PADs. By the same argument, photoelectrons with $E_p < U_p$ could not be observed in the experiment [8] because of the small $U_p \approx \omega$.

The momentum transfer to low-energy photoelectrons also depends on the ellipticity of the standing wave, as shown in

Fig. 3. For $\Lambda = -1$, the momentum transfer decreases when the ellipticity is increased and only one set of maxima remains for $\varepsilon > 0$. This is in contrast to high-energy photoelectrons, where the momentum transfer is larger for circular than for linear polarization [8]. For $\Lambda = +1$, no longitudinal momentum is transferred for circular polarization, since angular momentum conservation forbids the virtual Compton scattering. However, the momentum transfer is enhanced for elliptically polarized light with $\varepsilon = 0.5$ and $\Lambda = +1$: Low-energy photoelectrons are emitted with a high probability with large longitudinal momenta ($\Delta p_z \approx 1150\hbar k$). This is our second

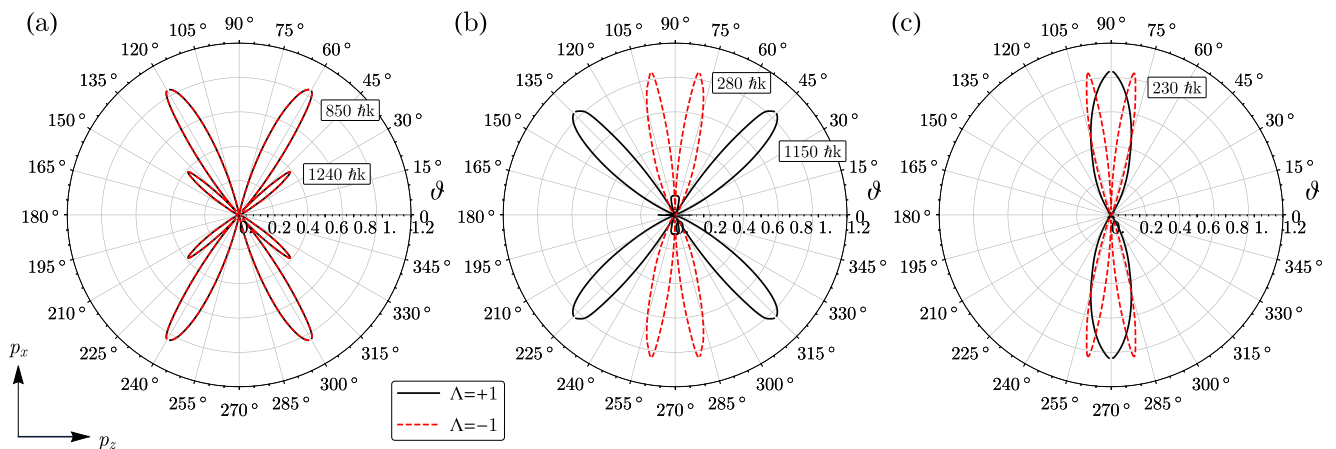


FIG. 3. PADs of low-energy photoelectrons ($E_p = 2.8 \text{ eV} \approx 0.7U_p$) for (a) linear, (b) elliptical, and (c) circular polarizations of the standing wave. Results are shown for standing waves with $I = 15 \times 10^{13} \text{ W/cm}^2$ and for both orientations $\Lambda = +1$ (black solid curves) and $\Lambda = -1$ (red dashed curves). All PADs are normalized to their respective maxima and the absolute magnitudes of the red dashed curves differ by a factor of (a) 1.0, (b) 0.33, and (c) 0.16, respectively, from the black solid curves. All other parameters are the same as in Fig. 2.

main result: The momentum transfer to low-energy photoelectrons can be controlled by a change of the ellipticity when all other laser parameters remain fixed. This is a consequence of the ellipticity dependence of the expansion coefficients $C_N(\mathbf{p})$ in the Volkov state (2) (cf. Appendix A). Physically, the ponderomotive force field acting on the photoelectron is strongly ellipticity dependent [28]. In future studies, it will be interesting to see how the momentum transfer, based on a semiclassical dynamics of the photoelectron in this force field, depends in detail on the polarization properties of the standing wave.

In summary, we have shown for the high-intensity KDE that low-energy photoelectrons can gain large longitudinal momenta and that these momenta can be controlled by the ellipticity of the standing wave. This large momentum transfer can be observed if the intensity of the standing wave exceeds a certain threshold I_{\min} that depends on the wavelength. Our results demonstrate that the high-intensity KDE provides a means to create low-energy photoelectrons with large and controllable longitudinal momentum. In the future, it will be an important task to include the Coulomb potential in the continuum in order to correctly describe the behavior of low-energy photoelectrons. It is known that the SFA used in the present work underestimates the yield of low-energy photoelectrons [29] and we therefore expect that the inclusion of the Coulomb potential may enhance the effect reported here. Furthermore, the standing wave may be modeled in a more realistic way using a Gaussian beam profile and a finite pulse duration. Within the formalism used here, this will yield more complex nondipole Volkov states and it is an interesting question how the theoretical results are then modified.

B.B. and W.P. acknowledge support from the Helmholtz Institute Jena and the Research School of Advanced Photon Science of Germany.

APPENDIX A: NONDIPOLE VOLKOV STATES

The nondipole Volkov states for a photoelectron in the laser fields (1) can be written in position space as [19]

$$\chi_{\mathbf{p}}(\mathbf{r}, t) = \frac{1}{(2\pi)^{3/2}} e^{-i(E_p t - \mathbf{p}\mathbf{r})} e^{-i\Gamma(\mathbf{r}, t)}, \quad (\text{A1})$$

with the photoelectron energy $E_p = p^2/2$ and the modified Volkov phase $\Gamma(\mathbf{r}, t)$ that depends on the explicit form of the vector potential. Evaluation of $\Gamma(\mathbf{r}, t)$ according to the procedure outlined in Ref. [19] and successive application of the Jacobi-Anger transform [30] yields

$$\chi_{\mathbf{p}}(\mathbf{r}, t) = \frac{1}{(2\pi)^{3/2}} \sum_{n_1, \dots, n_6 = -\infty}^{\infty} C_{n_1, \dots, n_6}(\mathbf{p}) \times e^{-i(E_{n_1, \dots, n_6} t - \mathbf{p}_{n_1, \dots, n_6} \mathbf{r})}, \quad (\text{A2})$$

with the expansion coefficients

$$C_{n_1, \dots, n_6}(\mathbf{p}) = J_{n_1}(\rho_1) J_{n_2}(\rho_2) J_{n_3}(\alpha_1^+) J_{n_4}(\alpha_2^+) J_{n_5}(2\alpha_{12}^+) \times J_{n_6}(2\alpha_{12}^-) e^{-in_1\theta_1} e^{-in_2\theta_2}, \quad (\text{A3})$$

where $J_m(x)$ are Bessel functions of the first kind, and the respective energies and momenta are given by

$$E_{n_1, \dots, n_6} = E_p - \alpha_1^- \omega_1 - \alpha_2^- \omega_2 - (n_1 + 2n_3 + n_5 + n_6)\omega_1 - (n_2 + 2n_4 + n_5 - n_6)\omega_2 \quad (\text{A4})$$

and

$$\mathbf{p}_{n_1, \dots, n_6} = \mathbf{p} - \alpha_1^- \mathbf{k}_1 - \alpha_2^- \mathbf{k}_2 - (n_1 + 2n_3 + n_5 + n_6)\mathbf{k}_1 - (n_2 + 2n_4 + n_5 - n_6)\mathbf{k}_2. \quad (\text{A5})$$

In order to better distinguish the two counterpropagating laser modes $A^{(1)}$ and $A^{(2)}$ forming the standing wave, we denoted their frequencies and wave vectors as ω_1 and ω_2 , and $\mathbf{k}_1 = k\mathbf{e}_z$ and $\mathbf{k}_2 = -k\mathbf{e}_z$, respectively. The constants appearing in the above expressions depend on the details of the vector potential and have the explicit form

$$\alpha_{1/2}^- = \pm \frac{U_p}{\omega_{1,2}} \frac{1}{p_z/c \mp 1}, \quad (\text{A6a})$$

$$\alpha_{1/2}^+ = \frac{\alpha_{1,2}^-}{2} \frac{1 - \varepsilon^2}{1 + \varepsilon^2}, \quad (\text{A6b})$$

$$\rho_{1/2} = \pm \frac{4U_p}{\omega_{1,2}\sqrt{1 + \varepsilon^2}} \frac{\sqrt{p_x^2 + \varepsilon^2 p_y^2}}{p_z/c \mp 1}, \quad (\text{A6c})$$

$$\theta_1 = -\Lambda\theta_2 = \arctan\left(\varepsilon \frac{p_y}{p_x}\right), \quad (\text{A6d})$$

$$\alpha_{12}^+ = \frac{1 + \Lambda\varepsilon^2}{1 + \varepsilon^2} \frac{4U_p^2}{p_z/c(\omega_1 - \omega_2) - (\omega_1 + \omega_2)}, \quad (\text{A6e})$$

$$\alpha_{12}^- = \frac{1 - \Lambda\varepsilon^2}{1 + \varepsilon^2} \frac{4U_p^2}{p_z/c(\omega_1 + \omega_2) - (\omega_1 - \omega_2)}. \quad (\text{A6f})$$

In short, we can write $N_1 = n_1 + 2n_3 + n_5$, $N_2 = n_2 + 2n_4 + n_5$, and $N_{12} = n_6$, and use that $\omega_1 = \omega_2 = \omega$ for the standing wave considered in the present work in order to obtain Eq. (2).

APPENDIX B: INFLUENCE OF THE TARGET POSITION

In our calculations, we consider a single atomic target that is placed on the beam axis at position $z = z_0$. A realistic experimental target, however, consists of a cloud of atoms distributed over some range $z_1 \leq z \leq z_2$ that also extends in the polarization plane. As a nonlinear process, the ATI depends strongly on the intensity of the laser field at the target position.

Since we model the counterpropagating laser modes forming the standing wave as plane-wave fields, the intensity does not depend on the x and y coordinates. Therefore, we consider a target placed on the beam axis. If the target is not placed at a node of the laser field ($z_0 = n\lambda/2$) for $\varepsilon = 0$, the PADs always exhibit the same qualitative behavior. Therefore, in our calculations, we always set $z_0 = \lambda/8$. This underestimates the momentum transfer for linearly polarized standing waves as measured in an experiment but will not change our main conclusions. For circular polarization, the results match the average distributions expected for a realistic cloud of atoms. In the discussion in the present work, it is therefore sufficient to make this approximation.

- [1] H. Batelaan, *Rev. Mod. Phys.* **79**, 929 (2007).
- [2] U. Eichmann, T. Nubbemeyer, H. Rottke, and W. Sandner, *Nature (London)* **461**, 1261 (2009).
- [3] S. Eilzer, H. Zimmermann, and U. Eichmann, *Phys. Rev. Lett.* **112**, 113001 (2014).
- [4] X. Ren, J. Zhang, Z. Xu, and D.-S. Guo, *Opt. Express* **19**, 24858 (2011).
- [5] P. L. Kapitza and P. A. M. Dirac, *Math. Proc. Cambridge Philos. Soc.* **29**, 297 (1933).
- [6] D. L. Freimund, K. Aflatooni, and H. Batelaan, *Nature (London)* **413**, 142 (2001).
- [7] D. L. Freimund and H. Batelaan, *Phys. Rev. Lett.* **89**, 283602 (2002).
- [8] P. H. Bucksbaum, D. W. Schumacher, and M. Bashkansky, *Phys. Rev. Lett.* **61**, 1182 (1988).
- [9] L. V. Keldysh, *J. Exptl. Theoret. Phys. (U.S.S.R.)* **47**, 1945 (1964) [*Sov. Phys. JETP* **20**, 1307 (1965)].
- [10] F. H. M. Faisal, *J. Phys. B: At. Mol. Phys.* **6**, L89 (1973).
- [11] H. R. Reiss, *Phys. Rev. A* **22**, 1786 (1980).
- [12] C. T. L. Smeenk, L. Arissian, B. Zhou, A. Mysyrowicz, D. M. Villeneuve, A. Staudte, and P. B. Corkum, *Phys. Rev. Lett.* **106**, 193002 (2011).
- [13] A. Ludwig, J. Maurer, B. W. Mayer, C. R. Phillips, L. Gallmann, and U. Keller, *Phys. Rev. Lett.* **113**, 243001 (2014).
- [14] B. Wolter, M. G. Pullen, M. Baudisch, M. Sclafani, M. Hemmer, A. Senfleben, C. D. Schröter, J. Ullrich, R. Moshhammer, and J. Biegert, *Phys. Rev. X* **5**, 021034 (2015).
- [15] D.-S. Guo and G. W. F. Drake, *Phys. Rev. A* **45**, 6622 (1992).
- [16] X. Li, J. Zhang, Z. Xu, P. Fu, D.-S. Guo, and R. R. Freeman, *Phys. Rev. Lett.* **92**, 233603 (2004).
- [17] C. Yu, J. Zhang, Z. Sun, J. Gao, and D.-S. Guo, *Frontiers Phys.* **10**, 104208 (2015).
- [18] L. Rosenberg and F. Zhou, *Phys. Rev. A* **47**, 2146 (1993).
- [19] B. Böning, W. Paufler, and S. Fritzsche, *Phys. Rev. A* **99**, 053404 (2019).
- [20] L. Rosenberg, *Phys. Rev. A* **49**, 1122 (1994).
- [21] R. Erhard and H. Bauke, *Phys. Rev. A* **92**, 042123 (2015).
- [22] M. M. Dellweg and C. Müller, *Phys. Rev. A* **95**, 042124 (2017).
- [23] X. Fang, K. F. MacDonald, E. Plum, and N. I. Zheludev, *Sci. Rep.* **6**, 31141 (2016).
- [24] J. Faure, C. Rechatin, A. Norlin, A. Lifschitz, Y. Glinec, and V. Malka, *Nature (London)* **444**, 737 (2006).
- [25] D. B. Milošević and W. Becker, *J. Mod. Opt.* **50**, 375 (2003).
- [26] E. Pisanty, D. D. Hickstein, B. R. Galloway, C. G. Durfee, H. C. Kapteyn, M. M. Murnane, and M. Ivanov, *New J. Phys.* **20**, 053036 (2018).
- [27] M. Førre, J. P. Hansen, L. Kocbach, S. Selstø, and L. B. Madsen, *Phys. Rev. Lett.* **97**, 043601 (2006).
- [28] P. W. Smorenburg, J. H. M. Kanters, A. Lassise, G. J. H. Brussaard, L. P. J. Kamp, and O. J. Luiten, *Phys. Rev. A* **83**, 063810 (2011).
- [29] C. I. Blaga, F. Catoire, P. Colosimo, G. G. Paulus, H. G. Muller, P. Agostini, and L. F. DiMauro, *Nat. Phys.* **5**, 335 (2009).
- [30] M. Abramowitz, *Handbook of Mathematical Functions, With Formulas, Graphs, and Mathematical Tables* (Dover, New York, 1974).